

Internal Swell: Distribution and Redistribution of Internal-Wave Energy

M. H. Alford

Applied Physics Laboratory and School of Oceanography, University of Washington, Seattle

Abstract. The spatial distribution and total power input to internal waves have now been computed for the wind and the tides. More relevant to ocean circulation is the distribution of internal-wave mixing, which can differ from the source distributions via long-range propagation. Here, 60 historical moored records are used to compute low-mode horizontal energy-flux in the near-inertial and tidal bands. The resultant sparse but global patterns are related to the source distribution for each band. It is found that near-inertial flux is overwhelmingly equatorward, as required for waves generated at the inertial frequency on a β -plane, and wintertime-enhanced, consistent with storm generation. Tidal flux is generally away from regions of strong topography. Flux in both bands is $O(1 \text{ kW m}^{-1})$, sufficient to radiate $O(15\text{-}50\%)$ of energy far from source regions.

1. Introduction

Our present picture of the Earth’s ocean circulation includes a vigorous Meridional Overturning Circulation (MOC), wherein $O(20\text{-}30)$ Sv ($=10^6 \text{ m}^3 \text{ s}^{-1}$) sink at high latitudes, and upwell diffusely at lower latitudes. Theoretical considerations (*Sandstrom*, 1908), profile fits (*Munk*, 1966; *Munk and Wunsch*, 1998), and inverse circulation models (*Ganachaud and Wunsch*, 2000) all suggest that vigorous turbulence is required in the ocean’s abyss to enable the upwelling portion of the cell; without it, the ocean would eventually fill with weakly-stratified, stagnant, dense water. Integrated globally, an estimated 2 TW ($1 \text{ TW}=10^{12} \text{ W}$) of power are required to fuel the turbulence (*Munk and Wunsch*, 1998, henceforth MW98). The issue is controversial, however, some arguing for less (*Webb and Sugimotohara*, 2001) or nearly none. In the rest of this paper, I will use expressions like “the required 2 TW” with the realization in mind that we still do not know whether the ocean is essentially diffusive or adiabatic!

This paper considers the ability of internal waves to supply the “needed” power, with an eventual goal of determining the distribution of the resultant mixing. The approach taken is to determine the distribution of energy input into the internal waves from their two primary sources (the wind and the tides), and then to map the horizontal energy flux associated to the subsequent propagating waves. With perfect knowledge of the sources, S , and the flux vector field, \vec{F}_{prop} , and in a time-invariant ocean, then the depth-integrated

internal-wave dissipation rate, D , is given by

$$D = S - \nabla \cdot \vec{F}_{prop}. \quad (1)$$

The calculation of the wind and tidal source terms has been done elsewhere, and is reviewed in section 2. Briefly, the wind appears to input 1 TW to the general circulation (*Wunsch*, 1998) and 0.5 TW to near-inertial motions (*Alford*, 2003b). About 0.7 TW of power is available to deep-water M_2 internal tides (and an extrapolated 1 TW to all tides) (*Egbert and Ray*, 1998). Together, there appears to be enough power to supply the needed 2 TW, and the spatial dependence of each source term is now known fairly well. However, altimetric (*Ray and Mitchum*, 1997) and tomographic (*Dushaw et al.*, 1995) observations have detected internal tides radiating far ($> 1000 \text{ km}$) from their sources. Circumstantial evidence suggests that near-inertial waves can also propagate far. For example, a low-latitude near-inertial wave propagated an estimated 350 km before mixing (*Alford and Gregg*, 2001c). Therefore, all power is clearly not dissipated where it is input. The question addressed in this work (and see also Lou St. Laurent’s paper, this volume) is, how much energy radiates far from sources, and how does this affect the resulting mixing distribution? Estimates of horizontal energy flux from 60 historical moored velocity and temperature records are used to address the question. Time series and statistics of the fluxes are presented in section 3, and (sparse) vector flux maps are plotted for each band atop the respective source term in section 4.1. Some

simple control-volume calculations are performed, indicating that a substantial fraction of the energy in both the near-inertial and the tidal band propagates significantly from its source.

2. Sources

2.1. Near-inertial Source Distribution

The wind efficiently generates ocean mixed layer motions at the inertial frequency, f . A simple slab mixed-layer model describes the ocean response very well (*Pollard and Millard, 1970*):

$$\frac{dZ}{dt} + (r + if)Z = \frac{T}{H}, \quad (2)$$

where $Z = u + iv$ is the mixed-layer current, $T = \rho^{-1}(\tau_x + i\tau_y)$ is the wind stress, and H is the mixed-layer depth. The damping coefficient, r , models the decay by propagation of the motions out of the region. Convergences in Z lead to vertical motions at the mixed-layer base, which force propagating motions. Brushing subtleties aside for the present discussion (*Alford, 2003b*), the flux is given by the vector product of the wind stress and a suitably-defined mixed-layer current: $\Pi = \vec{\tau} \cdot \vec{u}$

In a pioneering work, *D'Asaro (1985)* first solved (2) using wind data from a dozen National Data Buoy Center (NDBC) winds, and showed that the flux from the wind to the ocean is positive, wintertime-enhanced and intermittent. *Alford (2001)* solved (2) with Reanalysis winds from the National Center for Environmental Prediction (NCEP; 4x-daily, 2.5° resolution) and a mixed-layer-depth climatology (*Levitus and Boyer, 1994*) to obtain a near-global map of energy flux from the wind to the ocean. Based on buoy comparisons, he showed that the results were bias-free for latitudes $< 50^\circ$. He excluded regions poleward of there, since the NCEP and buoy solutions lost coherence as f approached the winds' Nyquist frequency (2 cpd). In an improved calculation, *Alford (2003b)* used a high-resolution regional atmospheric model to verify the high-latitude response, and extended the calculation to the poles. In addition, some shortcomings of (2) and the expression for the flux were addressed. Though all of these types of calculations are limited by the reliability of the wind product used, *Alford (2003b)* is the most accurate to-date. (By contrast, the *Watanabe and Hibiya (2002)* calculation is suspect for several reasons discussed in *Alford, 2003b*).

The spatial dependence of the flux is shown in Figure 1. Broad midlatitude and wintertime maxima demonstrate the dominance of travelling midlatitude storms in forcing near-inertial motions. As found by *D'Asaro (1985)*, a few events typically account for most of the flux at each location.

The globally integrated power input from the wind to the ocean is about 0.47 TW, about 1/4 of MW's 2 TW. Interestingly, the flux has increased by about 25% over the 54-year time span of the NCEP Reanalysis (Figure 2), paralleling increases in extratropical storm frequency and intensity in both the Northern (*Graham and Diaz, 2001*) and Southern hemispheres.

The wind also does work on the lower-frequency circulation. Computing $\vec{\tau} \cdot \vec{u}_g$ where \vec{u}_g is the geostrophic surface velocity from TOPEX/POSEIDON, *Wunsch (1998)* computed the work done by the wind on the oceanic general circulation, obtaining a total of 1 TW – mostly in the Southern Ocean. This energy is also potentially available to mix the deep ocean – but the energy pathways are as yet undiscussed. Energy is clearly lost from the general circulation to eddies, but the eddy decay process is not understood. One potential mechanism is radiation of near-inertial internal waves as eddies adjust geostrophically. This would constitute another near-inertial source, likely concentrated near fronts (e.g. Gulf Stream, Kuroshio, and the Southern Ocean), that is not considered here.

The wind-generated, mixed-layer motions excite full-ocean-depth propagating disturbances, and *Gill (1984)* showed that these can be described in terms of vertical modes, and that propagation was downward and equatorward. An insignificant fraction of the energy input is required to deepen the mixed-layer. The balance is available for propagating near-inertial waves. The one observation to estimate the near-inertial energy to leave the region was *D'Asaro et al. (1995)*, who estimated that 70% of the depth-integrated energy lost during 3 weeks was explainable by horizontal propagation. A key point is that the waves must propagate towards the equator where f is lower, since generation is at the latitudinal turning point: poleward propagation would cause evanescent waves of $\omega < f$.

2.2. M₂ Source Distribution

From several independent astronomical measurements, it is known that about 2.5 TW of energy are dissipated by the lunar tide. It was previously thought that nearly all of this was dissipated in bottom boundary layers in shallow seas, and thus irrelevant to abyssal mixing. However, theoretical calculations (*Sjöberg and Stigebrandt, 1992; Morozov, 1995*) began to show about 10 years ago that a significant fraction of this may be lost to internal motions generated in the deep sea as the barotropic tide flows over the sloping bottom. More recently, direct solutions to Laplace's tidal equations that assimilate TOPEX-POSEIDON sea-surface-height data have been rapidly improving, and support this finding. The conversion of barotropic energy to baroclinic mo-

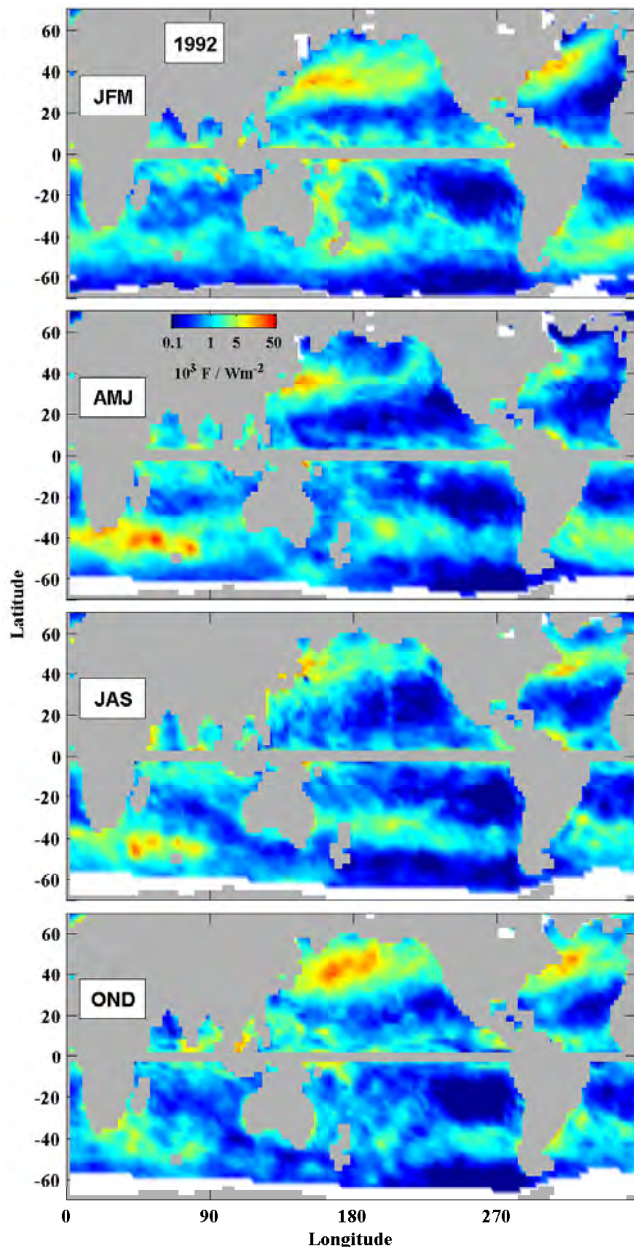


Figure 1. The 1992 global distribution of work done by the wind on near-inertial motions, incorporating monthly mixed-layer-depth variations. Each panel is a seasonal average over the months indicated at left. Ice is indicated in white.

tions is given as the divergence of the energy flux in the barotropic tide, in an expression analogous to 1. *Egbert and Ray* (2000) have presented maps of this (reproduced later in this paper), which show strong peaks near regions of strong topographic variation (e.g., Hawaii). Integrating globally, they obtain 0.7 ± 0.1 TW of deep-sea barotropic-baroclinic conversion for M2. With less certainty, the other tidal constituents can be extrapolated,

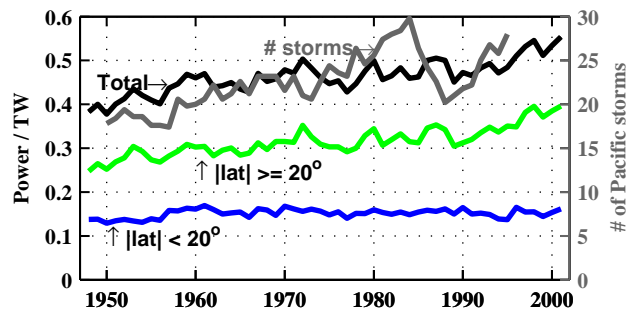


Figure 2. Time series from 1948-2001 of global dissipation due to near-inertial wind work integrated over the region equatorward (blue) and poleward (green) of 20° , and the total (black). Gray is the 5-year-running-mean number of North Pacific cyclones [*Graham and Diaz, 2001*].

for a total of ≈ 1 TW.

3. Fluxes

In this section, the flux calculation is demonstrated. The near-inertial and tidal-band fluxes are computed separately by band-pass filtering. (Note, however, that poleward of 50° , the semidiurnal and near-inertial bands overlap and are therefore inseparable!) Briefly, flux is computed as follows (see Appendix for details): vertical isopycnal displacement η is inferred from band-passed temperature records and climatological profiles (Figure 3a,b). A least-squares solution is obtained for the amplitude of the two longest-wavelength normal modes (Figure 3c) in terms of the discrete-depth moored measurements. Depth-integration yields the baroclinic pressure anomaly, p' , in terms of η . The correlation between velocity and p' equals the energy flux.

3.1. A Sample Near-Inertial Time Series

Typical time series of depth-integrated near-inertial flux (Figure 4a,b) show both positive and negative contributions, occurring in pulses of several days' duration and magnitude $O(10\text{-}30 \text{ kW m}^{-1})$. Magnitudes are much greater during the two (Southern) winters spanned (shaded). The time integral of each (c,d) indicates predominant wintertime propagation toward the northeast, and nearly no net flux during summertime (visible as zero slope), consistent with wintertime storm generation at $\omega \approx f$ and subsequent equatorward propagation.

3.2. Detailed Plots

To give more insight into the calculation, the near-inertial and tidal fluxes are plotted in more detailed form in Figures 5 and 6. These plots are preliminary

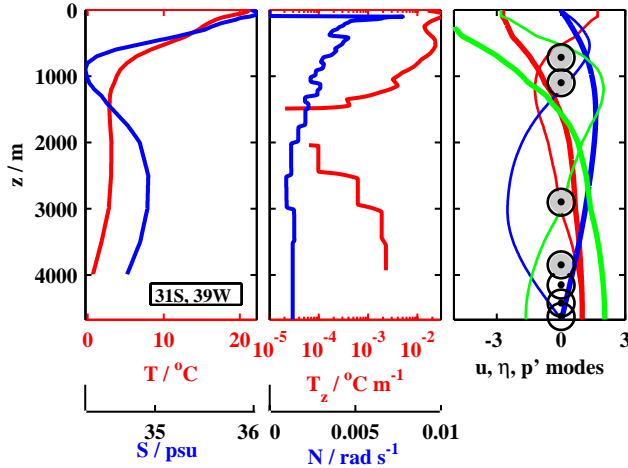


Figure 3. Hydrographic profiles, mode structure and instrument depths for a typical mooring. (a) Climatological temperature (red) and salinity (blue) profiles at the mooring location (31S, 39W). (b) Temperature gradient T_z (red) and buoyancy frequency, $N(z)$ (blue) computed from (a). (c) The first (thick) and second (thin) vertical normal modes of velocity, u (red), displacement, η (blue), and baroclinic pressure anomaly, p' (green). Circles indicate instrument depths. In this and all calculations, temperature measurements where $T_z < 3 \times 10^{-5} \text{ }^\circ\text{C m}^{-1}$, or where T increases towards the sea-floor, are removed from the calculation (bottom three records here).

and were not presented at the meeting, but offer a wealth of information:

- *Comparison of near-inertial and tidal fluxes.* Near-inertial flux (Figure 5,a-b) occurs in “bursts” of \approx one-week duration; by contrast, tidal flux is variable (Figure 6,a-b) but occurs in longer bursts (e.g. steady NW-ward M2 flux from yeardays 80-180). This finding is supported by probability density functions, presented below.
- *Signal-noise ratio.* The mode-1 and -2 amplitude magnitudes (panels c-e, red and black)) compared to the residual (green) indicate the periods when the signals are mostly consistent with a mode-1 and mode-2 inverse. All of the large flux events occur, of course, during large S/N.
- *Standing versus propagating waves.* In the top panes, the mode-1 amplitudes are plotted as hodographs for 10-day periods indicated below with gray shading. The top panes represent standard current ellipses, which are all highly circular since the frequency is close to f . The bottom two panels are “current-displacement” ellipses, where mode-

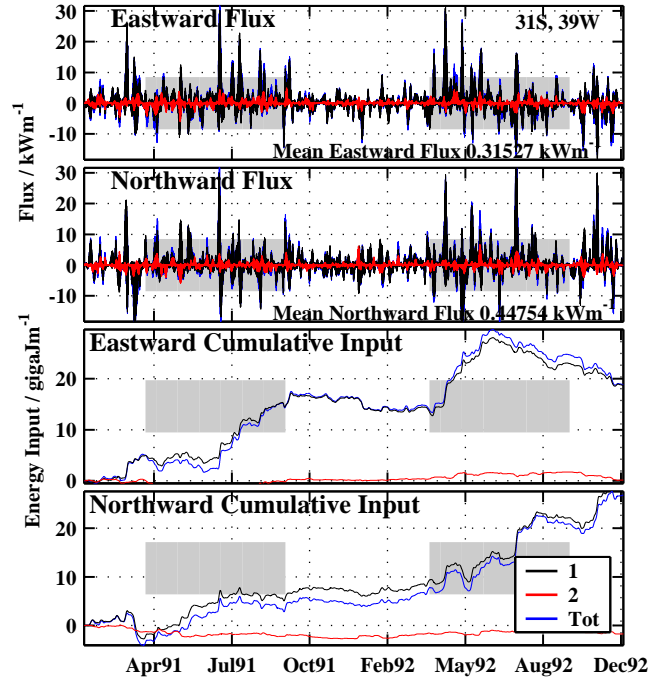


Figure 4. Typical near-inertial time series. (a,b) Depth-integrated eastward (a) and northward (b) energy flux in the near-inertial band for mode 1 (black), mode 2 (red), and the total (blue), from the mooring in Figure 1. Southern winter (defined as 1 Apr-30 Sep) is shaded. (c,d) The time-integral of panels (a,b), indicating cumulative energy passage. For this mooring, the flux is 1) wintertime-enhanced, 2) equatorward, and 3) dominated by mode-1.

1 current and displacement amplitudes are normalized by their maximum value during each 10-day period. Then, $u/|u|$ is plotted versus $\eta/|\eta|$ in the middle set of panes, and $v/|v|$ is plotted versus $\eta/|\eta|$ in the bottom set. A pure northward propagating wave has v and η (and thence p) in phase, indicated as highly elliptical v - η (e.g. Figure 5, yearday 668). Standing-wave motions have current and pressure in quadrature, resulting in circular $u\eta$ and no flux. The current ellipses are always consistent with the corresponding phase estimates (panels i,j,k). At times, ellipses span a period of changing phase, resulting in multiple ellipses (e.g. Figure 5, $v\eta$, yearday 498).

To take a tidal example, the broad period of SW-ward flux from yearday 80-180 (Figure 6a,b) maintains $\approx 180^\circ$ phase between both (u,η) and (v,η) , with corresponding elongated current-displacement ellipses. Based on these plots, large fluxes in both near-inertial and tidal bands generally have phase consistent with propagating

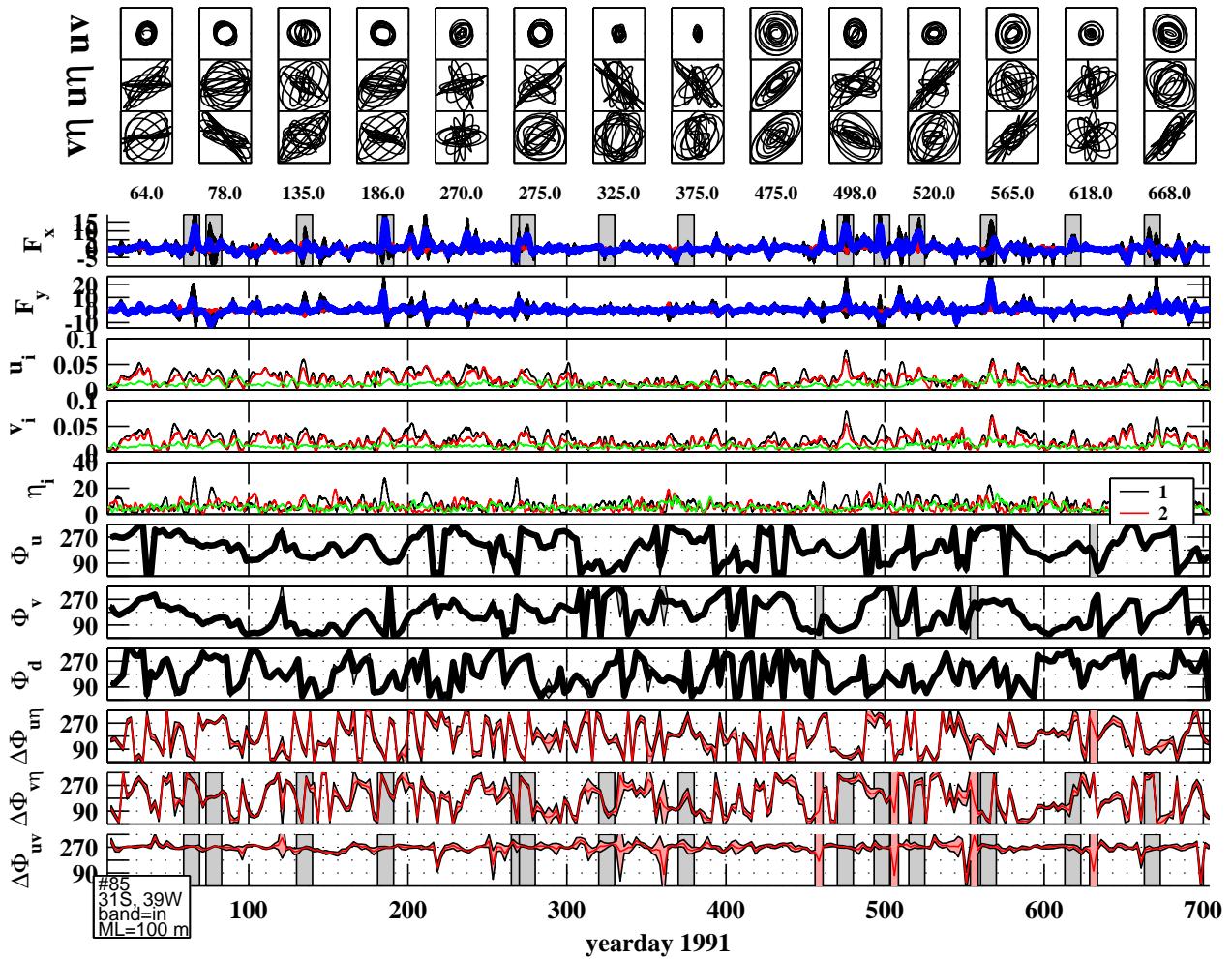


Figure 5. Time series of near-inertial flux, modal amplitude, ellipses and phase for the same mooring in figure 4. Yearday continues past 365 into the next year. Mode-1 ellipses of uv , $u\eta$ and $v\eta$ are plotted at top for selected 10-day periods, indicated on the time series below with vertical gray shading. (Note that the selected periods are not evenly spaced, and do not always line up with the ellipse plots.) The bottom 11 panels are time series of: (a,b) zonal and meridional flux (same as figure 4. (c,d,e) Modal amplitude magnitude for u , v and η . Black, red and green correspond to mode-1, mode-2 and the residual, respectively. (f,g,h) (Negative) GMT phase of u , v and η . Error bars are shaded. (i,j,k) Relative phase between u and η , v and η , and u and v . Phases are computed using harmonic analysis over overlapping 5-day windows.

waves. Many more examples must be examined from different locations.

- *Frequency.* The slow modulation of near-inertial phase may be used to determine frequency changes. The slow decrease in phase of near-inertial u and v from yearday 30-100 indicates a very slightly sub-inertial signal ($\Delta f = -.002$ cpd).

By contrast, tidal phase remains much more constant (as expected); comparison of these phases to surface-tide phases should offer much information on generation regions. Much work remains.

3.3. Probability Density Functions

As is the case for energy input by storms (*D'Asaro, 1985; Alford, 2001*) near-inertial energy passage occurs in finite bursts, with a few events accounting for much of the total (e.g., June 1991, April 1992). This is borne out in probability density functions (PDF's; Figure 7, blue) of all near-inertial flux estimates for all moorings, which exhibit long tails indicative of an intermittent process. These findings support the notion of internal-wave "groups" (*Thorpe, 1999*).

By contrast, the tidal-band fluxes (Figure 7, green) show more constant energy passage and shorter-tailed distributions, consistent with their more constant forc-

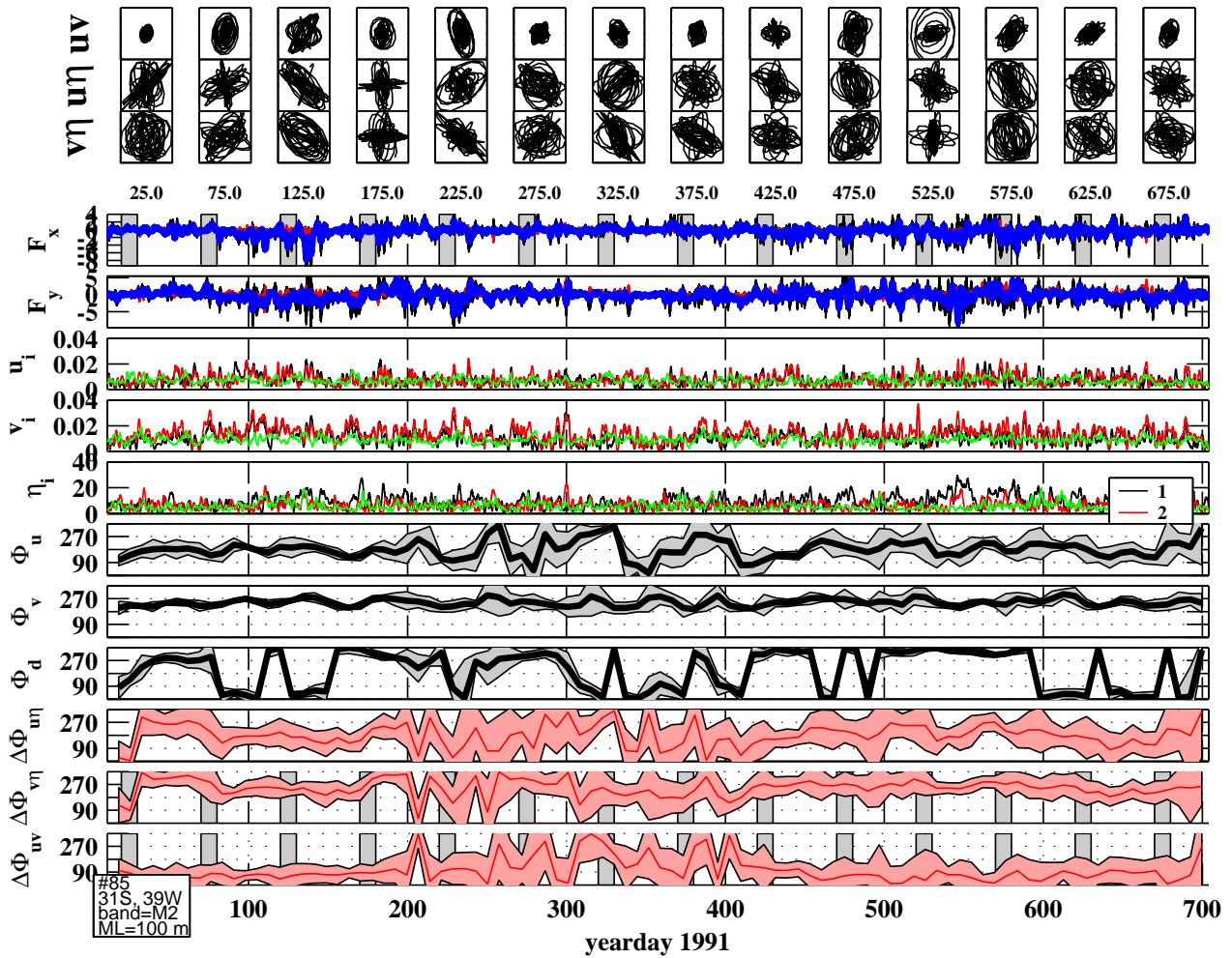


Figure 6. As in Figure 5 but for the semidiurnal band. Note that the phases are the negative of those in Figure 5, and the phases are computed over 14.5-day windows.

ing.

The PDF's also demonstrate the predominance of equatorward propagation for near-inertial waves but not for internal tides. This will also be apparent in global maps of the vector fluxes, next section.

4. Global Distribution of Sources and Fluxes

4.1. Maps

Annual-mean near-inertial fluxes in both hemispheres (Figure 8a) are directed overwhelmingly equatorward, as demonstrated in the histogram of poleward flux (inset), and generally away from regions of large energy input from the wind to near-inertial motions (color) (Alford, 2003a). In the North Pacific and North Atlantic, where coverage is denser, fluxes generally decrease in

magnitude toward the east, as do the wind-energy inputs. The zonal component of the fluxes is predominantly eastward, as expected given the predominance of eastward-travelling storms (D'Asaro *et al.*, 1995).

The tidal fluxes (Figure 8b) are generally directed away from internal-tide sources (Egbert and Ray, 2000). Examples include arrows emanating from the Western Pacific Trench, and north across the equator from the Tuamotu archipelago (Ray and Mitchum, 1998) at 20S, 220E and/or Micronesia/Melanesia, further west. Strong fluxes emanate from some continental shelves; e.g., northern Europe (also observed by (Pingree and New, 1991) and Cuba. Elsewhere (Brazil, U.S. west coast), propagation is on-shelf.

Northeastward energy radiation is observed along 150W at 25N and 40N, in agreement with altimetric estimates (Ray and Mitchum, 1998; Ray and Cartwright, 2001), which only detect mode-1, astronomically phase-

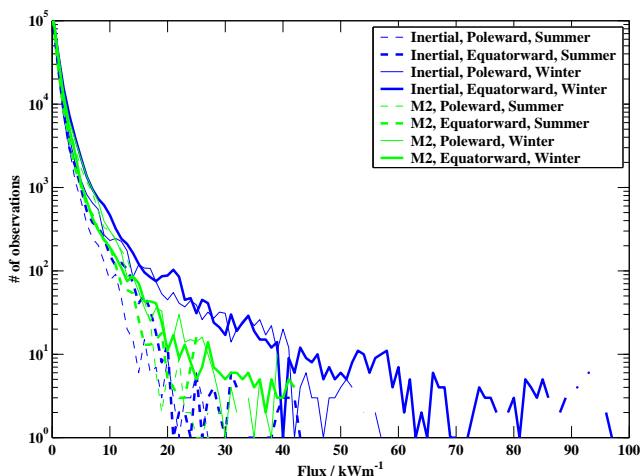


Figure 7. Histograms of meridional energy flux from near-inertial (blue) and tidal (green) bands, from all 60 moorings. Various traces (see legend) correspond to poleward/equatorward propagation and summer/winter periods.

locked signals. Strong northward fluxes are seen here well past where phase-locked fluxes have weakened, indicating that phase-locked signals may be a small fraction of the total. The weak flux observed further west at the BEMPEX site (41N, 163W) here and by *Ray and Cartwright* (2001) may result from superposition of northward fluxes from Hawaii and southward fluxes from the Aleutians, also suggested from altimetric estimates (*Ray and Mitchum*, 1998; *Ray and Cartwright*, 2001); *Cummins et al.*, 2001).

Coverage is fair in the North Atlantic and Pacific, but pitiful at low latitudes and in the Southern Hemisphere, particularly in the Pacific. Inclusion of all suitable data from the Woods Hole and British Oceanographic Data Centre archives would improve coverage in the North Atlantic, but would only provide a few more points in the Southern Ocean, and none in the South Pacific. Apparently, resolution of fluxes in these oceans must await new deployments (preferably “profiling moorings” (*Doherty et al.*, 1999) capable of resolving all modes). Several well-placed moorings would considerably improve the picture.

4.2. Budgets

In spite of the poor spatial coverage, a comparison of near-inertial fluxes to wind-energy inputs is computed for a control volume enclosing the Pacific storm track (Fig. 8a, box). An annual-mean energy input of 65 ± 10 GW (13% of the global total) is computed by integrating the wind-energy flux over the box. The 5 moorings spanning the box’s southern edge display a mean south-

ward flux of $\approx 1.5 \text{ kW m}^{-1}$, for a 12 GW energy loss rate due to near-inertial propagation across the box’s southern side. Based on these (admittedly few) moorings, at least 15-20% of the energy input propagates significantly from its source region. (Because the horizontal flux estimate may be low (see Methods), and the wind input is an upper bound on energy available for propagating waves, this percentage is a lower bound.) The remainder is dissipated locally either during generation or by breaking before the waves have left the box.

This 12 GW is available to fuel dissipation in the lower latitudes, where the wind forcing is much weaker. The associated breaking, if uniform over (0-30N, 150-230E), would yield a depth-mean dissipation rate $\approx 10^{-10} \text{ W kg}^{-1}$, typical of “background” thermocline mixing rates (*Gregg et al.*, 1987). The horizontal and vertical distribution of the mixing (not resolved) would depend on the waves’ interactions and propagation routes, and would be expected to have a strong seasonal cycle.

Similar calculations can be done for tidal propagation across control surfaces (Figure 8b) parallel to the Western Pacific Trench and the Hawaiian ridge source regions. Strong tidal flow across abrupt bottom features results in 45 ± 10 GW and 20 ± 5 GW (6.5% and 3% of the global total) of M2 internal-tidal production at these respective locations (*Egbert and Ray*, 2000). In the Western Pacific, the mean flux is 2 kW m^{-1} away from the region, indicating 10 GW ($\approx 25\%$) transmission eastward across the line. For Hawaii, the mean flux is $\approx 1 \text{ kW m}^{-1}$ to the NE for 3 GW ($\approx 15\%$) transmission across the line. For both volumes, the transmission out the other side is unmeasured; if symmetric, these percentages should be doubled, for 50% and 30%, respectively. Though uncertain, these numbers support other theoretical (*St. Laurent and Garrett*, 2001), modelling (*Merrifield and Holloway*, 2002); and observational (preliminary results from the Hawaii Ocean Mixing Experiment; E. Kunze, pers. comm) suggestions that much of internal-tidal energy leaves the source region (also St Laurent; this issue). The agreement in the tidal case with estimates by other methods lends confidence to the near-inertial estimates, for which no alternate method is available.

5. Discussion

This paper has presented estimates of the distribution and magnitude of the internal-wave source terms for the wind and the tides, and shown that their magnitudes are comparable to each other, and large enough to provide much if not all of the fabled 2 TW that compelling but unproven arguments suggest are necessary to maintain the stratification of the deep ocean. Ex-

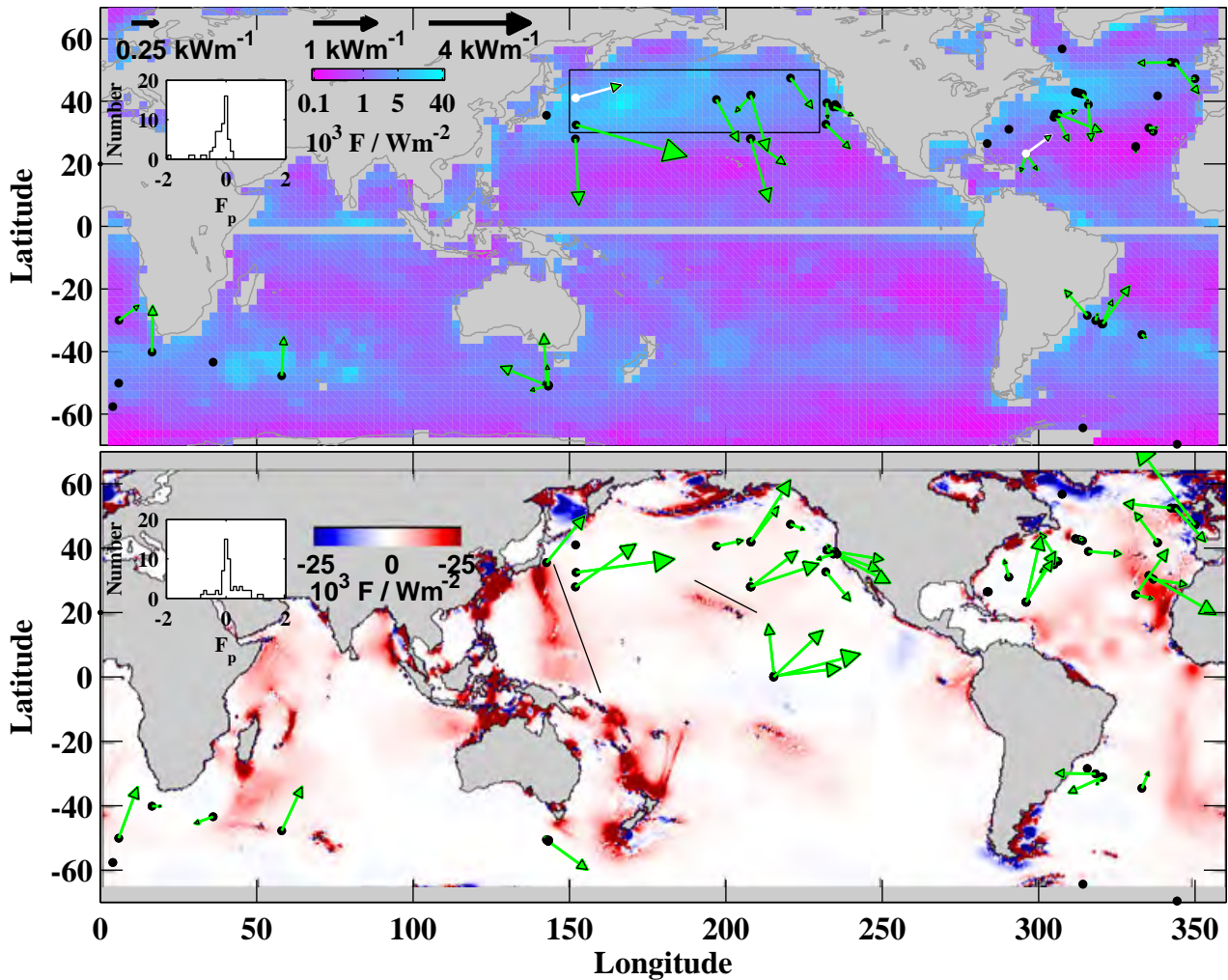


Figure 8. Source terms and energy-flux vectors. (a) Depth-integrated, annual-mean near-inertial energy-flux vectors for modes 1 and 2 from 60 historical moored records. The arrow lengths are logarithmic, with references indicated at upper left. Moorings with $|F| < 0.1 \text{ kW m}^{-1}$ appear as a black dot without an arrow. The few instances of poleward propagation are plotted in white. Colormap indicates annual-mean energy input from the wind to near-inertial mixed-layer motions (Alford, 2003b). The color scale is logarithmic and is indicated at upper left. (b) As in (a) but for the semidiurnal band. Colormap denotes internal-tide conversion using the TPXO.5 model, courtesy of G. D. Egbert. (Insets) Histogram of the poleward flux component for all moorings. Flux uncertainties (see Methods) are 50% (magnitude) and 30° (direction). For latitudes $|\lambda| > 50$ (e.g. northern European shelf), the frequency bands in (a) and (b) overlap, preventing their separation. The box and lines in the Pacific are discussed in the text.

tending a new technique (Kunze *et al.*, 2002) to vertically sparse moored data, the horizontal fluxes of internal waves are estimated in each frequency band (near-inertial for the wind; semidiurnal for the M2 tide). Sparse but global maps indicate that the fluxes in the two bands are 1) directed away from source-term maxima, 2) comparable in magnitude to each other and 3) sufficient to radiate substantial portions of the energy far from the sources. These findings are not surprising or new for the tides, which can be measured using other methods. The suggestion that near-inertial waves

can also propagate far, and may be as important as the tides to mixing the deep ocean, deserves further study.

The paper's title is an analogy with surface swell, which also occupies the lower-frequency end of the wave spectrum and can also propagate across ocean basins. With regard to the global internal-wave field, these results appear to support D'Asaro's suggestion at the 1991 Aha Hulikoa meeting that long-range internal-wave propagation can "smear out" the inhomogeneous sources into the remarkably spatially constant and isotropic internal-wave continuum (Garrett and Munk, 1975).

They also suggest that the near-inertial peak may result from equatorward propagation of energy generated at f (Garrett, 2001), rather than from poleward propagation of continuum energy to its latitudinal turning point (Fu, 1981). However, given the excellent agreement of Fu’s model with data at the locations available at that time, a revisit of Fu’s analysis seems called for, armed with new data and new ideas.

Many details are completely unaddressed here, including: non-linear interactions between near-inertial waves, tides, and the rest of the continuum; refraction by mesoscale eddies; and bottom and surface interactions. All of these will govern the ray paths and ultimately the depth distribution of the internal-wave mixing. In addition, generation of near-inertial waves via geostrophic adjustment (*a la* Kunze and Sanford, 1984) must be examined. The hope is that progress will result by comparison of these “direct” internal-wave flux estimates with both emerging theoretical pictures of internal-wave field (Muller’s Internal-Wave Action model, this issue), and the growing database of mixing observations at different locations.

Acknowledgments. This work was funded by the Office of Naval Research Young Investigator award, grant #N00014-02-1-0526. I am indebted to Eric D’Asaro, Eric Kunze and Chris Garrett for insights and discussions, and to Maya Whitmont for quality control and preparation of the mooring data.

Appendix A: Flux Calculation

A1. Data selection

1064 moorings were examined, that were deployed from 1973-2000 and archived by the Oregon State University Buoy Group (I also thank Doug Luther for the BEMPEX mooring). Only 60 satisfied the following criteria: ≥ 4 instruments of which the first was shallower than 800 m and the deepest < 1000 m from the bottom; sampling interval ≤ 3 hour; water depth $H \geq 3200$ m; record length ≥ 180 days, spanning at least one winter; and no excessive mooring motion (evident as coherent measured temperature and pressure).

A2. Band-pass filtering

Flux was computed separately for the near-inertial and semidiurnal bands via band-pass filtering. A 4th-order Butterworth filter was designed with zero-phase response, and quarter-power points at $\{c^{-1}\omega_c, c\omega_c\}$ around a center frequency $\omega_c = \{f, M2\}$. The bandwidth parameter, $c = 1.25$, was chosen narrow enough to maximally isolate the two bands, while wide enough to avoid filter “ringing.” For this value, motions in the near-inertial and tidal bands are separable for latitudes $\lambda < 50$. Poleward of this, the frequency ranges overlap (i.e., $cf > c^{-1}M_2$), and their motions cannot

be distinguished.

A3. Computing Vertical Displacement from Temperature

Climatological hydrographic data (Levitus and Boyer, 1994) were used to compute vertical temperature gradient $T_z(z)$ and buoyancy frequency $N(z)$ at each mooring location (example in Figure 3a,b). Vertical displacement is computed via

$$\eta(z_j, t) = T(z_j, t)T_z^{-1}(z_j), \quad (A1)$$

where $T(z_j, t)$ is the band-passed temperature at depth z_j and time t . This assumes that temperature signals are due to vertical advection of a constant gradient past the mooring.

Advection of horizontal gradients by the inertial and tidal currents also contribute to η . An inertial current of ± 0.1 m s $^{-1}$ at latitude 30° has horizontal displacements of $\pm \approx 2$ km. Horizontal gradients on this scale change sign frequently; therefore, the resultant fluxes average out. Only the components of η caused by a wave-like motion acting against a quasi-constant gradient produce significant fluxes. (Large-scale meridional temperature gradients, which could bias these measurements, yield negligible false vertical displacements of < 1 m.)

A4. Modes

Over a flat bottom, the exact vertical structure of internal waves can be represented by a superposition of discrete vertical modes (Figure 3c) that depend only on the buoyancy frequency, $N(z)$. For low-frequency waves ($\omega \ll N$) over a flat bottom, these are the solutions to

$$\frac{\partial^2}{\partial z^2} \eta_i(z) + c_i^{-2} N^2(z) \eta_i(z) = 0 \quad (A2)$$

subject to the boundary conditions $\eta(0) = \eta(H) = 0$, where c_i are the eigenspeeds and H is the water depth. The modal expressions for velocity (\mathbf{u}), displacement (η) and pressure anomaly (p') are simply related to all simply related to each other via the internal-wave polarization relations.

Full-depth profiles of modal velocity, $u_i(z, t)$, and displacement, $\eta_i(z, t)$, are obtained, for the first two modes, from the filtered time series $u(z_j, t)$ and (z_j, t) at discrete depths z_j , by performing a least-squares inverse at each time t . The resulting time series of modal amplitude typically rotate inertially (clockwise/counterclockwise in the northern/southern hemisphere) with small residual errors.

A5. Flux

The baroclinic pressure anomaly in each mode, p_i , is obtained by depth-integrating $N^2 \eta_i(z)$ and subtracting the mean (Kunze *et al.*, 2001). The baroclinic energy flux in each mode is then given by $\bar{F}_i = \langle \bar{u}_i p_i \rangle$, where $\langle \rangle$ indicates an average over a wave period. Only the depth-integrated flux, $\int_{-H}^0 F_i dz$, which has units of kW m $^{-1}$, is discussed here.

A6. Errors

There are various subtleties with both the estimation and interpretation of single-point energy-flux measurements, and a careful assessment of the various errors involved is still in progress (Nash and Alford, in preparation). Sources of error include spatial dependencies, modal interactions, mooring motion, and aliasing of unresolved modes onto the mooring geometry. (Energy flux is dominated by the lowest modes (Kunze *et al.*, 2002), as in Figure 2; Higher-mode ($i > 2$) motions are aliased onto the resolved modes, introducing errors.) For the present work, a sensitivity study was conducted where incoming waves of known structure and flux were passed through typical mooring geometries. Simulations using various reasonable stratifications, modal content, and instrument locations indicate that for typical 4-instrument moorings, the 2-mode estimates fall between 65% and 100% of the fully-resolved flux. The flux estimates are therefore 1) biased somewhat low if higher-mode input is present and 2) uncertain by O(50%). (High-mode wave inputs with antinodes near the instrument depths can cause the 2-mode solutions to be overestimates. Highly focussed internal-wave rays (Pingree and New, 1991; Lien and Gregg, 2000) would therefore be very poorly measured; however, it is unlikely that these are common enough in the deep sea to significantly affect these results.)

Since tidal forcing varies little (except though varying background stratification and currents), the spread in tidal-flux estimates at collocated moorings are another estimate of the method's intrinsic uncertainty. Conservative values of 50% and 30° are taken for the magnitude and directional uncertainties, consistent with the error estimates from the simulations. (The 4 moorings on the equator show similar magnitudes but considerable angular spread. Here, refraction by equatorial currents may be stronger.)

References

- Alford, M. H., and M. C. Gregg, Near-Inertial Mixing: Modulation of Shear, Strain and Microstructure at Low Latitude, *J. Geophys. Res.*, *106*, C8, 16,947–16,968, 2001.
- Alford, M. H., Internal swell generation: The spatial distribution of energy flux from the wind to mixed-layer near-inertial motions, *J. Phys. Oceanogr.*, *31*, 2359–2368, 2001.
- Alford, M. H., Redistribution of energy available for ocean mixing by long-range propagation of internal waves, *Nature*, *423*, 159–162, 2003a.
- Alford, M. H., Improved global maps and 54-year history of wind-work on ocean inertial motions, *J. Geophys. Res. Lett.*, *30*, 10.1029/2002GLO16614, 2003b.
- Cummins, P. F., J. Y. Cherniawski, and M. G. G. Foreman, orth Pacific internal tides from the Aleutian Ridge: Altimeter observations and modelling, *J. Mar. Res.*, *59*, 167–191, 2001.
- D'Asaro, E., The energy flux from the wind to near-inertial motions in the mixed layer, *J. Phys. Oceanogr.*, *15*, 943–959, 1985.
- D'Asaro, E., C. E. Eriksen, M. D. Levine, P. Niiler, C. A. Paulson, and P. V. Meurs, Upper-ocean inertial currents forced by a strong storm, I, Data and comparisons with linear theory, *J. Phys. Oceanogr.*, *25*, 2909–2936, 1995.
- Doherty, K. W., D. E. Frye, S. P. Liberatore, and J. M. Toole, A moored profiling instrument, *J. Atmos. Ocean. Tech.*, *16*, 1816–1829, 1999.
- Dushaw, B., B.D. Cuornelle, P. F. Worcester, B.M. Howe, and D. S. Luther, Barotropic and baroclinic tides in the Central North Pacific Ocean determined from long-range reciprocal acoustic transmissions, *J. Phys. Oceanogr.*, *25*, 631–647, 1995.
- Egbert, G. D., and R. D. Ray, Significant dissipation of tidal energy in the deep ocean inferred from satellite altimeter data, *Nature*, *405*, 775–778, 2000.
- Fu, L-L., Observations and Models of Inertial Waves in the Deep Ocean, *Rev. Geophys. Space Phys.*, *19*, 141–170, 1981.
- Ganachaud, A., and C. Wunsch, Improved estimates of global ocean circulation, heat transport and mixing from hydrographic data, *Nature*, *408*, 453–456, 2000.
- Garrett, C., What is the “near-inertial” band and why is it different from the rest of the internal wave spectrum?, *J. Phys. Oceanogr.*, *31*, 962–971, 2001.
- Garrett, C. J. R., and W. H. Munk, Space-time scales of internal waves: A progress report, *J. Geophys. Res.*, *80*, 291–297, 1975.
- Gill, A. E., On the behavior of internal waves in the wake of a storm, *J. Phys. Oceanogr.*, *14*, 1129–1151, 1984.
- Graham, N., and H. Diaz, Evidence for Intensification of North Pacific Winter Cyclones since 1948, *J. Climate*, *82*, 869–1893, 2001.
- Gregg, M. C., Diapycnal mixing in the thermocline, *J. Geophys. Res.*, *92*, 5249–5286, 1987.
- Kunze, E., L. Rosenfield, G. Carter, and M. C. Gregg, Internal waves in Monterey submarine canyon, *J. Phys. Oceanogr.*, *32*, 1890–1913, 2002.
- Kunze, E., and T. B. Sanford, Observations of near-inertial waves in a front, *J. Phys. Oceanogr.*, *14*, 566–581, 1984.
- Levitus, S., and T. Boyer, *World Ocean Atlas 1994*, NOAA Atlas NESDIS 4, U.S. Department of Commerce, Washington, D.C., 1994.
- Lien, R. C., and M. C. Gregg, Observations of turbulence in a tidal beam and across a coastal ridge, *J. Geophys. Res.*, *106*, 4575–54591, 2000.
- Merrifield, M.A., and P. E. Holloway, Model estimates of M2 internal tide energetics at the Hawaiian Ridge, *J. Geophys. Res.*, *107*, 10.1029/2001JC000996, 2002.
- Morozov, E. G., Semidiurnal wave global field, *Deep-Sea Res.*, *42*, 135–148., 1995.
- Munk, W. H., Abyssal Recipes, *Deep-Sea Res.*, *13*, 707–730, 1966.
- Munk, W., and C. Wunsch, Abyssal Recipes II: energetics of tidal and wind mixing, *Deep-Sea Res. Part I*, *45*, 1977–2010, 1998.
- Nash, J., and M. H. Alford, Interpretation of baroclinic energy fluxes: subtleties of estimates, in preparation, 2003.
- Pingree, R. D., and A. L. New, Abyssal Penetration and Bottom Reflection of Internal Tidal Energy in the Bay of Biscay, *J. Phys. Oceanogr.*, *21*, 28–39, 1991.

- Ray, R. D., and D. E. Cartwright, Estimates of internal tide energy fluxes from Topex/Poseidon altimetry: Central North Pacific, *Geophys. Res. Lett.*, *28*, 1259–1262, 2001.
- Ray, R. D., and G. T. Mitchum, Surfest manifestations of internal tides in the deep ocean: observations from altimetry and island gauges, *Prog. Oceanogr.*, *40*, 135–162, 1997.
- Sandstrom, J., Dynamische versuche mit meerwasser, *Ann. Hydrogr. Mart. Met.*, *36*, 6–23, 1908.
- Sjöberg, B., and A. Stigebrandt, Computations of the geographical distribution of the energy flux to mixing processes via internal tides and the associated vertical circulation in the ocean, *Deep-Sea Res. Part A*, *39*, 269–291, 1992.
- St. Laurent, L., and C. Garrett, The role of internal tides in mixing the deep ocean, *J. Phys. Oceanogr.*, *32*, 2882–2899, 2001.
- Thorpe, S. A., On the breaking of internal waves in the ocean, *J. Phys. Oceanogr.*, *29*, 2433–2441, 1999.
- Watanabe, M., and T. Hibiya, Global Estimates of the wind-induced energy flux to inertial motions in the surface mixed layer, *Geophys. Res. Lett.*, *29*, 22, 80.1–4, 2001GL014422, 2002.
- Webb, D. J., and N. Suginohara, Vertical Mixing in the Ocean, *Nature*, *409*, 37, 2001,
- Wunsch, C., The work done by the wind on the oceanic general circulation, *J. Phys. Oceanogr.*, *28*, 2332–2340, 1998.
-
- This preprint was prepared with AGU’s L^AT_EX macros v4, with the extension package ‘AGU++’ by P. W. Daly, version 1.6b from 1999/08/19.

